ADVANCED FUNCTIONAL MATERIALS
www.afm-journal.de

Mesoporous Colloidal Superparticles of Platinum-Group Nanocrystals with Surfactant-Free Surfaces and Enhanced Heterogeneous Catalysis

*Yongxing Hu, Yuzi Liu, and Yugang Sun**

Synthesis of colloidal superparticles (CSPs) of nanocrystals, a class of assembled nanocrystals in the form of colloidal particles, has been emerging as a new frontier in the field of nanotechnology because of their potential novel properties originated from coupling of individual nanocrystals in CSPs. Here, a facile approach is reported for the controlled synthesis of mesoporous CSPs made of various platinum-group nanocrystals that exhibit high colloidal stability and ligand-free surfaces to significantly benefit their applications in solution-phase heterogeneous catalysis. The synthesis relies on self-limiting growth of composite particles through coprecipitation of both Pt-group nanocrystals (or their precursor compounds) and silver halides on sacrificial substrates of colloidal silver particles. The intermediate silver halides in the composite particles play the critical role in limiting the continuous growth (and/or coalescence) of individual Pt-group nanocrystals and they can be selectively dissolved to create nanoscale pores in the resulting CSPs.

1. Introduction

Formation of colloidal superparticles (CSPs) from assembly of nanoparticles becomes interesting recently because CSPs represent a new class of potential building blocks for making functional materials useful in applications such as sensing,[1] photonics,[2] optoelectronics,[3,4] photovoltaics,[5] and biological separation.[6] Due to the existence of hierarchical nanostructures with bimodal length scales in single particles, the CSPs exhibit not only chemical and physical properties inherited from their constituent nanoparticles but also unique collective properties induced by coupling between their constituents.[7,8] The most successful strategy developed for the synthesis of CSPs relies on precisely guided self-assembly of presynthesized nanoparticles with well-controlled size (size distribution), shape, composition, and surface chemistry. The driving force for self-assembly originates from solvent evaporation, polymer templating, electrostatic interaction, hydrogen bonding, and/or interfacial tension.[9–17] For example, induced solvophobic interactions between surfactant and solvent molecules have been demonstrated in Cao's group to promote the production of shape-controlled CSPs from self-assembly of nanocrystals.[4,18–21] Another method developed in Li's group adopts microemulsion oil droplets as confined templates, within which nanoparticles undergo self-assembly to form CSPs upon the evaporation of low-boiling-point solvents in the microemulsion.[6,22–24] The self-assembly methods have achieved great success in synthesizing CSPs made of a large number of nanocrystals with different shapes and compositions. The resulting CSPs exhibit significantly enhanced performance in terms of magnetic properties and optical properties[25] in comparison with individual constituent nanocrystals. Unfortunately the most important property of nanocrystals, i.e., high surface areas, no longer exists in these CSPs because the gaps between individual nanocrystals are occupied with surfactant molecules that are critical for guiding self-assembly of nanocrystals. Although the surfactant molecules can be removed through calcination at elevated temperature,[22] this high-temperature process is always detrimental to maintain the nanocrystals and the mesoscopic structures of the CSPs. Alternatively, deposition of surfactant molecules on the surfaces of individual nanocrystal domains can be avoided by using the one-step processes, which integrate the synthesis of nanocrystals and their aggregation into CSPs in a single step. Examples have been demonstrated by Yin[26] for Fe_3O_4 CSPs and by Kotov et al.[11] for various semiconductor CSPs and semiconductor-Au core–shell CSPs. However, the nanocrystals with clean surfaces always undergo entropy-driven aggregation to coalescence and fuse together to reduce the surface energy as well as surface area.

Here, using Pt-group metals as an example, we demonstrate a method based on self-limiting growth of metal nanocrystals (or nanocrystal precursor compounds) in composite CSPs by simultaneous precipitation of metal nanocrystals and silver halides in the course of oxidative etching of colloidal Ag particles. In contrast to the previously reported CSPs, the Pt nanocrystals in the synthesized composite CSPs are surfactant-free and separated by silver halides to prevent the Pt nanocrystals from continuous growth and coalescence/fusion. The silver halides can be selectively dissolved at very mild condition (e.g., dilute ammonia hydroxide solution at room temperature) to leave nanoscale pores between the essentially intact Pt nanocrystals in the CSPs. The mesoscopic porosity in combination with

Dr. Y. Hu, Dr. Y. Liu, Dr. Y. Sun
Center for Nanoscale Materials
Argonne National Laboratory
9700 South Cass Avenue, Argonne, IL 60439, USA
E-mail: ygsun@anl.gov

DOI: 10.1002/adfm.201403664

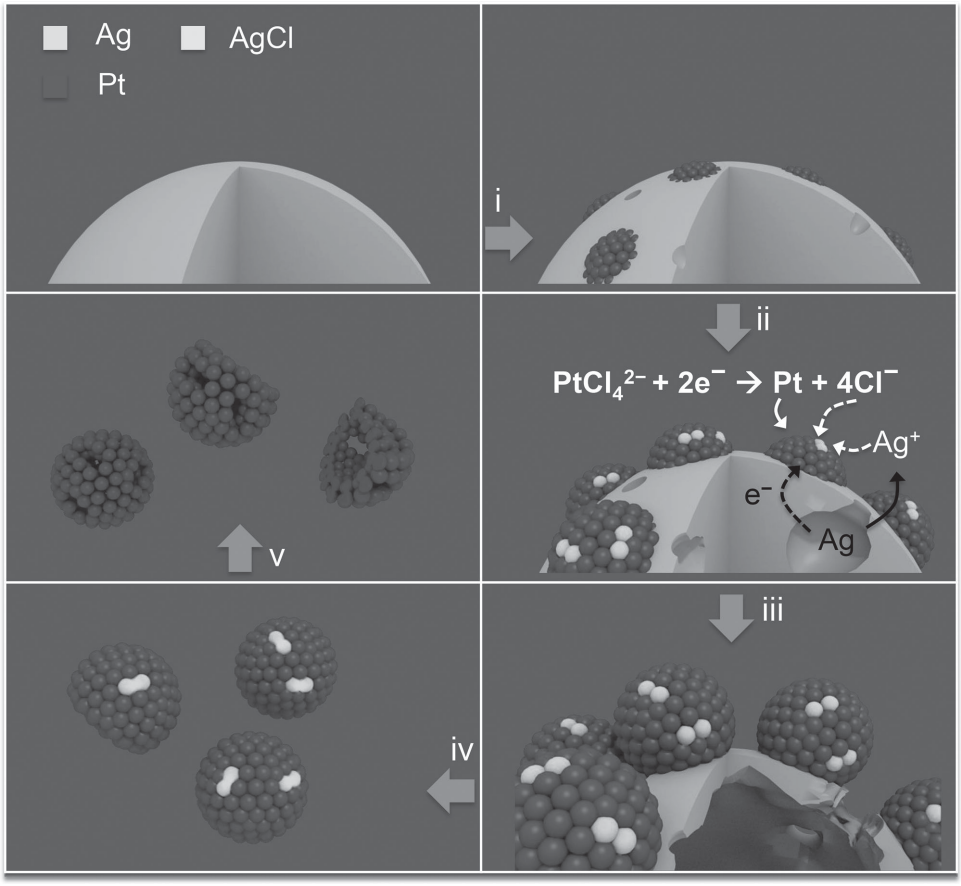

Figure 1. Schematic illustration of the major steps involved in the synthesis of porous CSPs made of Pt nanocrystals. Pt nanocrystals are generated from the galvanic reaction between $PtCl_4^{2-}$ and colloidal Ag particle substrates (step i). Due to the low solubility of AgCl, the Ag^+ and Cl^- ions produced from the galvanic reaction spontaneously form solid AgCl that coprecipitates with the Pt nanocrystals on the Ag particle substrates to form composite Pt–AgCl CSPs (steps ii and iii). The galvanic reaction gradually dissolves the Ag particles to release the Pt–AgCl composite CSPs into the reaction solution (step iv). AgCl in the freestanding Pt–AgCl composite CSPs is selectively dissolved with ammonia hydroxide to form porous Pt CSPs (step v).

the surfactant-free surfaces enables the high surface areas of individual Pt nanocrystals in the CSPs, which can be fully accessed to benefit applications such as catalysis.

2. Results and Discussion

2.1. Synthesis and Characterization of CSPs Made of Pt Nanocrystals

Surfactant-free CSPs consisting of Pt nanocrystals with porous features can be synthesized through the coprecipitation of Pt and AgCl nanocrystals in the course of redox reaction between sacrificial colloidal Ag substrates and $PtCl_4^{2-}$ ions. **Figure 1** schematically illustrates the major steps involved in the formation of porous Pt CSPs. The synthesis starts with the preparation of Ag colloidal particles that serve as sacrificial substrates to promote reduction of $PtCl_4^{2-}$ ions. Addition of an aqueous solution of Na_2PtCl_4 in a boiling aqueous dispersion of Ag particles initiates the galvanic replacement reaction to form Pt atoms and dissolve the Ag particles into Ag^+ ions.[27] The resulting Pt atoms prefer to condense into Pt nanocrystals on the surfaces of the Ag particles to minimize their surface energy. At the same time, free Cl^- ions are released from $PtCl_4^{2-}$ and precipitate with the dissolved Ag^+ ions when the local solubility product of Cl^- and Ag^+ excesses the K_{sp}^{AgCl} near the Ag particles' surfaces. Since there is no surfactant in the reaction solution, the resulting AgCl nanocrystals prefer to coprecipitate with the Pt nanocrystals to form Pt–AgCl composite CSPs extending from the surface of Ag particles. The coprecipitation prevents the Pt nanocrystals from growing into large crystals because the direct contact between AgCl and Pt can significantly interfere the growth of Pt crystalline lattices. Continuous reaction leads to the enlargement of the Pt–AgCl composite CSPs rather than the formation of new CSPs on the etched, and yet highly reactive, Ag surfaces, producing CSPs with a domelike morphology. When the Ag particles are completely consumed by the reaction, the Pt–AgCl composite CSPs are released into the reaction solution. Incubation of the composite CSPs with an aqueous solution of ammonium selectively dissolves AgCl, and the leftover Pt nanocrystals slightly relax and reorganize to form porous CSPs. No surfactant is used throughout the entire synthesis, which ensures the surfaces of final CSPs are free of organic ligands.

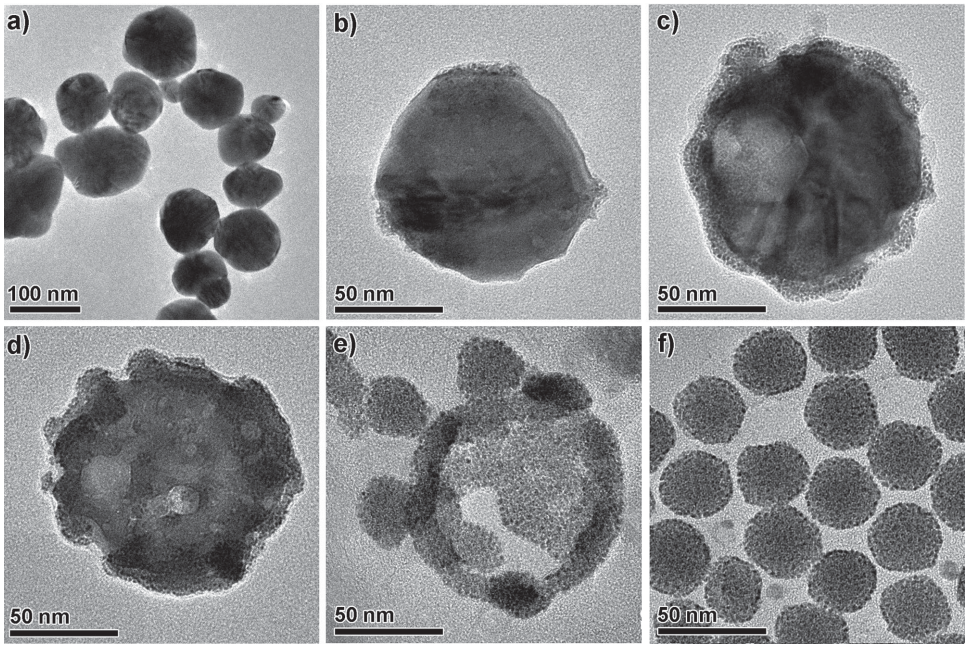

Figure 2. Representative TEM images of the products formed at different stages in the course of galvanic reaction between colloidal Ag particles and Na_2PtCl_4 in an aqueous solution. a) TEM image of the colloidal Ag particles that were synthesized with acetonitrile and citrates as capping molecules. b) TEM image of a Ag particle right after the galvanic reaction was initiated. c,d) TEM images of typical individual Ag particles after the Ag particles were partially etched, showing the formation of Pt–AgCl domelike bumps on the Ag particles. e) TEM image of the product formed when the Ag particles were almost dissolved, showing that the Pt–AgCl domelike bumps enlarged and started to release to form freestanding Pt–AgCl CSPs in the reaction solution. f) Typical TEM image of purified freestanding composite Pt–AgCl CSPs.

Figure 2 presents a series of representative transmission electron microscopy (TEM) images of the products formed at different reaction stages, which clearly highlight the major processes illustrated in Figure 1. The starting Ag particles (Figure 2a) were synthesized with small surfactant molecules (e.g., acetonitrile and citrates), which could not strongly bonded to the Ag surfaces and can be partially removed after washing the Ag particles for several times. The resulting nonuniformly covered Ag surfaces could then react with $PtCl_4^{2-}$ ions continuously. The reaction initiated the etching of the Ag particles at those spots with the highest surface energy and the produced Pt atoms nucleated and grew into nanocrystals at the sites with low surface energy (e.g., the positions decorated with tiny dots in Figure 2b). When more $PtCl_4^{2-}$ ions were added to the reaction solution, the Ag particles were selectively dissolved to form voids and the resulting Pt nanocrystals and AgCl nanocrystals were assembled on the surfaces of Ag nanoparticles to form domelike bumps (Figure 2c,d). Dissolution of the Ag nanoparticles was confirmed by the gradual change of surface plasmon resonance during the reaction (Figure S1, Supporting Information). Once the Ag nanoparticles were completely dissolved, the domelike composite assemblies of Pt and AgCl nanocrystals (i.e., Pt–AgCl CSPs) fell off from the cracked Ag surfaces (Figure 2e) and became freestanding in the reaction solution (Figure 2f). In some cases, if the density of CSPs on the surface of individual Ag particles was too high, they could touch (or possibly merge with) each other to form wavy shell-like particles that can prevent the CSPs from being dissociated and dispersed in the solution (Figure S2, Supporting Information). The large shell particles could be easily removed through a self-sedimentation on the basis of their significant difference in gravity compared to the freestanding CSPs, leaving pure composite Pt–AgCl CSPs in the solution (Figure 2f). The formation of Pt–AgCl CSPs was independent of morphologies of Ag particle substrates (Figure S3, Supporting Information). According to the process shown in Figures 1 and 2, the CSPs can be formed only when multiple Pt nanocrystals simultaneously nucleate and grow on the surface of the templating Ag nanoparticles. When the starting Ag nanoparticles are too small (e.g., <10 nm), the small surface area of single Ag nanoparticles cannot support the simultaneous nucleation and growth of multiple Pt nanocrystals as well as the assembly of them into CSPs on individual Ag nanoparticles. For example, quick reduction of $AgNO_3$ with $NaBH_4$ in the presence of poly(vinyl pyrrolidone) (PVP) and citrate can result in the formation of Ag nanoparticles with diameter of 5.6 ± 3.9 nm.[28] The reaction between obtained Ag nanoparticles and Na_2PtCl_4 only leads to individual Pt nanocrystals and small clusters consisting of only several Pt nanocrystals (Figure S4, Supporting Information). In addition, formation of dispersed freestanding CSPs became difficult in the presence of excessive surfactant in the reaction solution (Figure S5, Supporting Information). In addition, large amount of surfactant molecules adsorbed on the surface of the Ag particles can form uniform surface chemistry, leading to uniformly nucleate and grow composite Pt–AgCl shells around the Ag particles. These control experiments clearly indicate that using Ag particles with nonuniform surface passivation as source precursor is critical for success in the synthesis of high-quality CSPs as shown in Figure 2f.

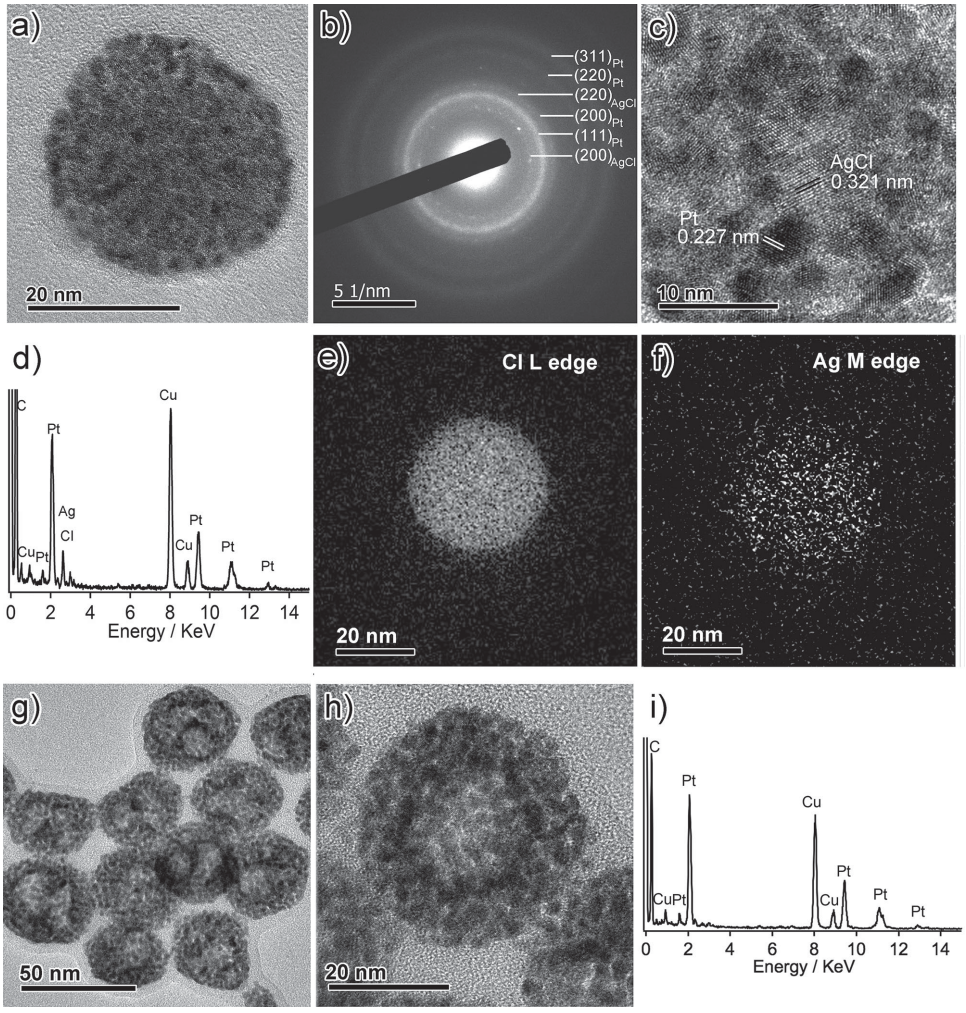

Figure 3. Structural characterizations of composite Pt–AgCl CSPs. a) Typical TEM image and b) SAED pattern of a single Pt–AgCl CSP with a maximum lateral dimension of ≈34 nm. c) HRTEM image of a Pt–AgCl CSP showing lattice fringes of both Pt and AgCl nanocrystals. The fringes with *d*-spacing of 0.227 nm of the darker dots correspond to Pt(111) lattices planes of the Pt. The fringes with *d*-spacing of 0.321 nm of the brighter areas correspond to AgCl(111) lattices. d) EDS spectrum recorded from an assembly of many Pt–AgCl CSPs, clearly showing the strong signals of Pt, Ag, and Cl. Signals of Cu, C, and O originated from the TEM grid. e,f) EFTEM images of the CSP shown in a) by using e) Cl L-edge (200 eV) and f) Ag M-edge (450 eV). g) Representative TEM image of porous Pt CSPs obtained after selective removal of AgCl from the composite Pt–AgCl CSPs. h) Enlarged TEM image of a single porous Pt CSP. The brighter contrast in the central region of the 2D projection indicates that the Pt nanocrystals form a quasi-shell particle due to slight reorganization during removal of AgCl. i) EDS spectrum recorded from an assembly of many porous Pt CSPs, clearly showing the absence of Ag and Cl in the sample.

The purified CSPs are uniform in their lateral dimensions and exhibit nearly identical appearance in electron microscopy images (Figures 2f and S6, Supporting Information). Although most of the Pt–AgCl CSPs show nearly circular projections, their actual morphology is described as hemispherical domes with flat bottoms (Figure S7, Supporting Information). **Figure 3**a presents a typical TEM image of a Pt–AgCl CSP with a projection diameter of ≈34 nm. It is clearly observed that the CSP consists of uniform nanocrystals with an average diameter of 3.02 ± 0.29 nm dispersed in a polycrystalline matrix with less imaging contrast. The polycrystalline nature of each CSP has been revealed by selected area electron diffraction (SAED). The SAED pattern can be indexed to two sets of diffraction patterns corresponding to Pt nanocrystals and AgCl nanocrystals (Figure 3b). The set of broad rings originate from reflections of (111), (200), (220), (311) lattices in face-centered cubic (fcc) Pt, indicating small dimension and random orientations of the Pt nanocrystals in individual CSPs. The other set of weak rings decorated with scattered bright spots are consistent with the (200) and (220) reflections of fcc AgCl lattices. The corresponding high-resolution TEM (HRTEM) image (Figure 3c) reveals that the nanocrystals with higher imaging contrast are made of Pt and the rest nanocrystals with lower imaging contrast are made of AgCl. X-ray diffraction (XRD) pattern of the CSPs also confirms the existence of both crystalline Pt and AgCl compositions (Figure S8, Supporting Information). Energy-dispersive X-ray spectroscopy (EDS) verifies that the as-synthesized SPs are composed of Pt, Ag, and Cl with atomic concentrations of 51.4%, 10.8%, and 37.8%, respectively (Figure 3d). The atomic ratio of Cl to Ag is significantly larger

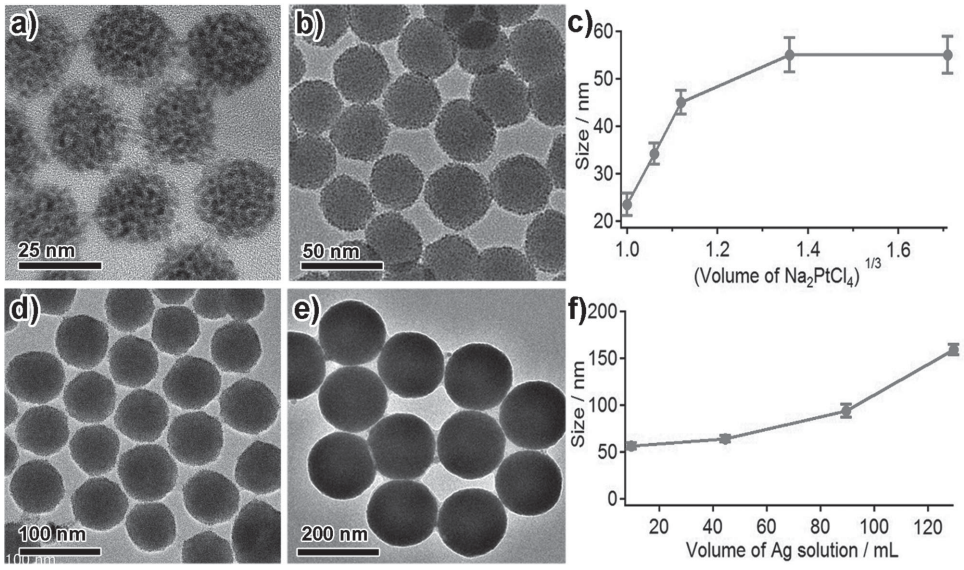

Figure 4. Size control over the composite Pt–AgCl CSPs. a–c) Size control was realized by tuning the volume of aqueous Na_2PtCl_4 solution. a,b) TEM images of two samples of CSPs with sizes of a) 23.5 and b) 45 nm that were synthesized according to this strategy. The volumes of Na_2PtCl_4 solution used for synthesizing CSPs shown in (a,b) were 1 and 1.4 mL, respectively. c) Plot of the relationship between the size of CSPs and the volume of Na_2PtCl_4 solution. d–f) Size control was realized by changing the volume of the starting Ag particle dispersion. d,e) TEM images of two samples of CSPs with sizes of d) 62 and e) 157 nm that were synthesized according to this strategy. The volumes of the starting Ag particle dispersion used for synthesizing CSPs shown in (d,e) were 45 and 130 mL, respectively. f) Plot of the relationship between the size of CSPs and the volume of the starting Ag particle dispersion.

than the stoichiometric ratio in AgCl crystals, implying that excessive Cl^- ions are adsorbed on the CSPs. Energy-filtered transmission electron microscopy (EFTEM) images of the CSP recorded at the Ag M-edge (450 eV) and the Cl L-edge (200 eV) in Figure 3e,f clearly show that both Ag and Cl well distribute throughout the CSP, suggesting that the crystalline AgCl fills the spaces around Pt nanocrystals in the CSP. The much stronger intensity of Cl signal than that of Ag is attributed to the existence of high concentration of adsorbed Cl^- ions on the CSP. The adsorbed Cl^- ions are critical to stabilize the composite CSPs in polar solvents (e.g., water, ethanol, etc.) since no organic surfactant molecules are used in the synthesis (Figure S9, Supporting Information). The surface Cl^- anions render the CSPs to be highly negatively charged with a Zeta potential of –35.6 ± 3.7 eV. These negative charges prevent the CSPs from aggregation, resulting in an increased stability and dispersibility in polar solvents. No obvious particle aggregation is observed when an aqueous dispersion of the Pt–AgCl composite CSPs is stocked for more than one year at room temperature.

Porous Pt CSPs with exposed surfaces of the Pt nanocrystals can be generated by dissolving the AgCl via incubation of the composite CSPs in an aqueous ammonium solution. It has been confirmed by TEM images (Figure 3g,h) that the porous Pt CSPs essentially retain the size and morphology of the parent Pt–AgCl composite CSPs. The small voids left by dissolving AgCl nanocrystals may coalescence/reorganize into larger voids, forming porous Pt CSPs with hollow interiors. EDS spectrum (Figure 3i) and XRD pattern (Figure S10, Supporting Information) of the porous Pt CSPs prove that AgCl nanocrystals are completely dissolved and Pt nanocrystals represent the only component of the porous CSPs. The porous Pt CSPs also exhibit high stability in polar solvents and the Zeta potential is measured to be –24.2 ± 3.1 eV. Similar to the Pt–AgCl composite CSPs, the porous Pt CSPs are not contaminated with organic surfactant (Figure S11, Supporting Information) and their ligand-free surfaces with increased accessibility show great potential to achieve improved performance in applications such as catalysis or sensing.

2.2. Size Control of the CSPs

Since the formation of CSPs on the colloidal Ag substrates follows the typical nucleation/growth mechanism,[29] we can conveniently tailor the size of CSPs by tuning either the total amount of the Pt precursor or the volume of the starting Ag particle dispersion, both of which can influence the kinetics involved in the nucleation and growth processes. For example, Pt–AgCl composite CSPs with sizes ranging from 23.5 to 55 nm have been successfully synthesized by simply varying the total amount of Na_2PtCl_4 added to a fixed aqueous dispersion of Ag particles. **Figure 4**a,b presents typical TEM images of two different CSP samples synthesized with adding 1 and 1.4 mL of 0.01 M Na_2PtCl_4 solution, respectively. Figure 4c summarizes the relationship between the size of the CSPs and the volume of Na_2PtCl_4 solution used in the synthesis. It has been revealed that the size of the CSPs cannot reach smaller than 23 nm because smaller sized CSPs are not stable enough to fall off from the Ag colloidal substrate. Preparation of CSPs with sizes larger than 55 nm is also difficult by only tuning the added volume of Na_2PtCl_4 solution because the galvanic reaction stops upon the complete consumption of colloidal Ag substrates regardless of the amount of Na_2PtCl_4 added to the reaction solution. This limitation can be overcome by changing

the starting volume of the colloidal Ag substrates while keeping the concentration and injection rate of the Na_2PtCl_4 solution constant. As a result, the actual concentration of Na_2PtCl_4 in the reaction solution at the initial nucleation stage can be further lowered if a larger volume of colloidal Ag substrates is used, leading to the formation of a lower concentration of nuclei and a possibility of forming larger CSPs. Figure 4d,e highlights the TEM images of CSPs with sizes of 62 and 157 nm synthesized by using 45 and 128 mL of the Ag particle dispersion, respectively. The dependence of the size of CSPs on the initial volume of Ag particle dispersion is plotted in Figure 4f, showing that larger CSPs can be achieved with the larger volume of Ag colloidal dispersion. Regardless of their sizes, the as-synthesized Pt–AgCl CSPs exhibit narrow size distributions (Figure S12, Supporting Information), which could be ascribed to the well-separated nucleation and growth process associated with the slow injection of Na_2PtCl_4 solution (at a rate of 10 μL s^{-1}). The size of the Pt nanocrystals only slightly increases from 2.6 to 3.2 nm when the size of CSPs increases from 23 to 157 nm (Figure S13, Supporting Information). In contrast, interconnected fractal structures are produced if the Na_2PtCl_4 precursor solution is quickly added to the dispersion of colloidal Ag particles (Figure S14, Supporting Information). Therefore, the size of Pt–AgCl composite CSPs (as well as the corresponding porous Pt CSPs) can be easily tuned over a broad range by carefully controlling the volumes of either Na_2PtCl_4 solution or Ag particle dispersion. The synthesis can be scaled up to produce CSPs with the quality similar to those shown in Figure 4 (Figure S15, Supporting Information).

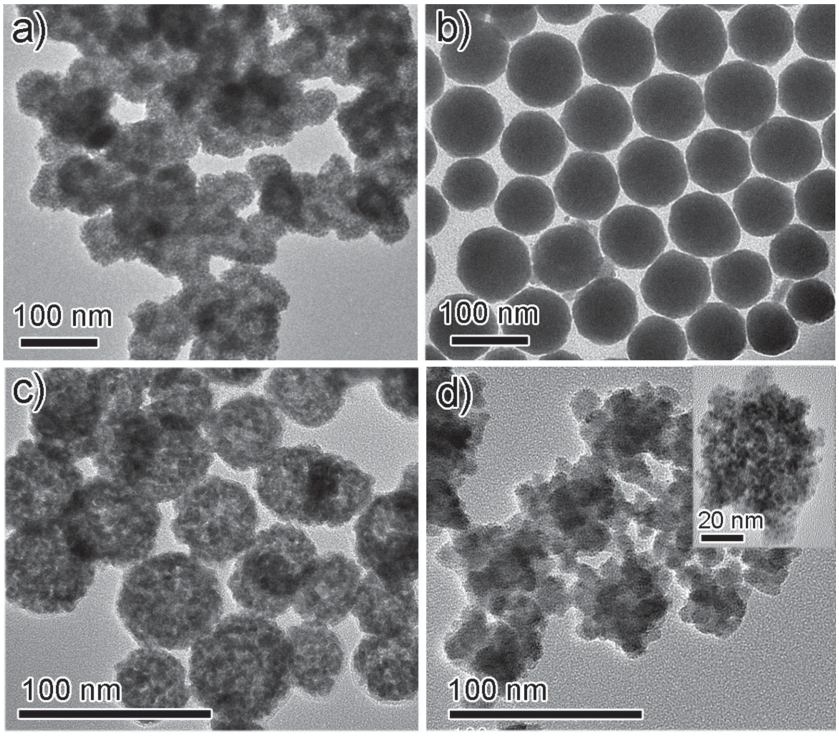

Figure 5. Representative TEM images of porous CSPs made of other Pt-group nanocrystals. a) TEM image of porous Pd CSPs with slight aggregation. b,c) TEM images of b) amorphous RhI_3–AgI composite CSPs and the corresponding porous crystalline Rh CSPs. d) TEM image of IrI_3–AgI composite CSPs and the corresponding porous crystalline Ir–AgI CSPs (inset).

2.3. Synthesis of CSPs Made of Other Pt-Group Metals

The strategy highlighted in Figure 1 can be easily extended to synthesize CSPs made of Pd nanocrystals by using Na_2PdCl_4 to react with colloidal Ag particles. In addition to directly react with Ag particles, $PdCl_4^{2-}$ ions tend to hydrolyze to form PdO nanocrystals at the reaction temperature (i.e., ≈100 °C), generating composite CSPs consisting of Pd nanocrystals, AgCl nanocrystals, and PdO nanocrystals (Figure S16a–c, Supporting Information). Existence of PdO in the composite CSPs causes the interconnection between each CSP to form chain-like structures. In order to convert the composite CSPs to porous Pd CSPs as shown in **Figures 5**a and S16d, Supporting Information, they are soaked with an aqueous solution of ammonium to dissolve the AgCl nanocrystals. The following solvothermal treatment in ethanol at 150 °C and a pressure of 41 psi can reduce PdO to nanocrystalline Pd. The resulting porous Pd CSPs retain the chain-like morphology and are composed of 98.3 at% Pd and trace amount of adsorbed Cl^- ions that help stabilize the Pd CSPs in polar solvents (Figure S16d,e, Supporting Information). The porous Pd CSPs exhibit good crystallinity with an fcc lattice (Figure S16f, Supporting Information).

Replacing Na_2PtCl_4 with either Na_3RhCl_6 or Na_3IrCl_6 cannot oxidize Ag colloidal particles under the reaction conditions for the synthesis of Pt–AgCl CSPs shown in Figure 2f. However, addition of KI to the reaction solutions can boost the oxidation due to the much lower solubility of AgI than AgCl.[30] In this case, the Ag particles are oxidized by oxygen (from air) to form AgI (Figure S17, Supporting Information). Meanwhile $RhCl_6^{3-}$ and $IrCl_6^{3-}$ ions can be transformed to solid species, i.e., RhI_3 and IrI_3, respectively, through anion exchange. Coprecipitation of different metal iodides leads to the formation of composite CSPs. For example, composite CSPs of RhI_3–AgI are shown in Figure 5b, displaying their uniform size and smooth surfaces (Figure S18a,b, Supporting Information). EDS and X-ray photoelectron spectroscopy (XPS) analysis confirms that these CSPs are composed of RhI_3 and AgI (Figure S18c,e,f, Supporting Information). These CSPs have poor crystallinity without specific lattice reflections in electron diffraction patterns (Figure S18d, Supporting Information). RhI_3 and AgI can be reduced with an aqueous solution of $NaBH_4$ to form Rh–Ag metallic CSPs (Figure S19, Supporting Information) and their crystallinity can be further improved through a solvothermal treatment in ethanol at 150 °C and a pressure of 40 psi for 20 min (Figure S20, Supporting Information). The resulting porous Rh CSPs (Figure 5c) are crystallized in fcc lattices and contain only trace amount of Ag (6%) and I (2%). In addition to porous

Rh CSPs, IrI_3–AgI composite CSPs containing trace amount of AgCl adopt dendritic shapes rather than spherical shape with smooth surfaces (Figures 5d and S21, Supporting Information). HRTEM image (Figure S21b, Supporting Information) and XRD pattern (Figure S21c, Supporting Information) reveal that AgI in the IrI_3–AgI CSPs are in the format of nanocrystals, which is different from the amorphous format in the RhI_3–AgI CSPs shown in Figure 5b. The amorphous IrI_3 can be reduced through a solvothermal treatment with ethanol to form Ir nanocrystals, which are attached to the AgI nanocrystals in the CSPs (inset of Figure 5d and Figure S22, Supporting Information). Presence of AgI nanocrystals is important to maintain the CSP structures by stabilizing and supporting the Ir nanocrystals. When AgI nanocrystals are completely reduced through the solvothermal treatment, the newly formed small Ir nanocrystals are too scattered to reconstruct into stable Ir CSPs similar to the porous Rh CSPs. These examples clearly show the importance of silver halides (e.g., AgCl and AgI) in limiting the continuous growth or coalescence of nanocrystals of Pt-group metal (or corresponding compounds) into monolithic domains in the composite CSPs, which benefits the formation of porous CSPs of Pt-group nanocrystals by selectively removing the silver halides from the composite CSPs. In principle, this strategy can be extended to the synthesis of composite CSPs from coprecipitation of two types of components, one of which can be selectively removed at mild conditions that do not significantly influence the properties of the other component.

2.4. Application of Porous Pt CSPs in Solution-Phase Heterogeneous Catalysis

Materials containing Pt represent the most commonly used catalysts for many commercially important reactions such as cyclopropanation, Suzuki coupling, and electron transfer reaction.[31–33] Platinum-based nanoparticles are more attractive because they can serve as catalysts to promote heterogenous catalysis that can benefit recycling of catalysts at the end of reaction. The challenge is to keep large surface areas of the nanoparticle catalysts accessible by the reaction species. In general, the capping species that help stabilize the small catalysts can strip off during the reactions, leading to aggregation of the nanoparticles and decrease of their surface areas. To solve this problem, supporting substrates such as polymers, carbon compounds, silica, or alumina are usually used to prevent aggregation of nanoparticle catalysts.[34] However, the supporting substrates would block partial surfaces of the catalysts and may involve in the reactions to influence the catalytic performance.[35] In addition, the catalytic activity of Pt nanoparticles also depends on how the Pt nanoparticles are immobilized on the supporting substrates.[36] Recently, porous Pt nanostructures with large lateral dimensions turn to be promising catalyst candidates in terms of their improved stability, the more active surface areas accessible by reaction species, as well as the recycling ability through simple centrifugation. For example, the assembly of chemically synthesized nanoparticles into network architectures has been proven to exhibit enhanced catalytic activity in comparison with the original monodispersed Pt nanoparticles.[37,38] Despite of this enhancement, there is still a room to further improve the catalytic performance if the capping species can be removed from the Pt nanostructures. Although conventional thermal annealing can burn away the capping species from the assembled porous architectures, it can sinter the Pt nanoparticles and greatly decrease the porosity in the architectures. In contrast, our synthesized porous CSPs made of nanocrystals of platinum-group metals (e.g., Pt, Pd, Rh, and Ir) exhibit surfactant-free surfaces, large accessible surface areas, and great stability in polar solvents. These advantages are beneficial for significantly enhancing their performance in applications such as catalysis in comparison with the conventional nanocrystals with surfactant capping layers and the previously reported CSPs. As a proof of concept, the porous Pt CSPs shown in Figure 4a have been used to catalyze an electron-transfer reaction involved in the reduction of hexacyanoferrate (III) ($Fe(CN)_6^{3-}$) with thiosulfate ions ($S_2O_3^{2-}$).[33] The electron transfer reaction between hexacyanoferrate (III) and sodium thiosulfate reaction has been used widely for investigating the catalytic activity of metal nanostructures owing to two important properties: the reaction does not occur without a catalyst and the catalyzed reaction can be monitored easily. Eighty eight percent of $Fe(CN)_6^{3-}$ ions were reduced when the reaction lasted 35 min. In contrast, using same amount of poly(acrylic acid) (PAA)-capped Pt nanocrystals (with sizes of 3 nm) as catalyst converted only 40% of $Fe(CN)_6^{3-}$ ions to $Fe(CN)_6^{4-}$ ions even when the reaction lasted over 100 min (**Figure 6**). The results showed that the reaction rate of the catalytic reactions greatly increased in the presence of the porous Pt CSPs composed of Pt nanocrystals with similar size of the PAA–Pt nanocrystals. The two Pt nanostructures showed different catalytic activity, which could be attributed to the different accessible surface area of these nanostructures. The porous Pt CSPs can be easily recovered via centrifugation while the PAA-capped Pt nanocrystals are extremely difficult (or even impossible) to recover from the reaction solution (Figure S23, Supporting Information). These distinct differences clearly demonstrate the promise of the porous platinum-group metal CSPs in high-performance catalysis.

3. Conclusion

A generalized strategy has been developed for the synthesis of mesoporous CSPs made of nanocrystals of platinum-group metals (e.g., Pt, Pd, Rh, and Ir) through self-limited growth of both metal nanocrystals (or precursors) and silver halide in individual colloidal particles. The silver halide components can be selectively dissolved to expose the surfaces of individual metal nanocrystals in the CSPs. By controlling the reaction conditions, the size and composition of the CSPs can be easily tuned. For example, the Pt CSPs with sizes ranging from 20 to 150 nm have been synthesized by varying the ratio of Na_2PtCl_4 (i.e., precursor of Pt) and the sacrificial Ag nanoparticle precursor. This strategy can be extended to the synthesis of composite CSPs from coprecipitation of two types of components, one of which can be selectively removed at mild conditions that do not significantly influence the properties of the other component to form mesoporous CSPs. The as-prepared mesoporous CSPs are free of organic

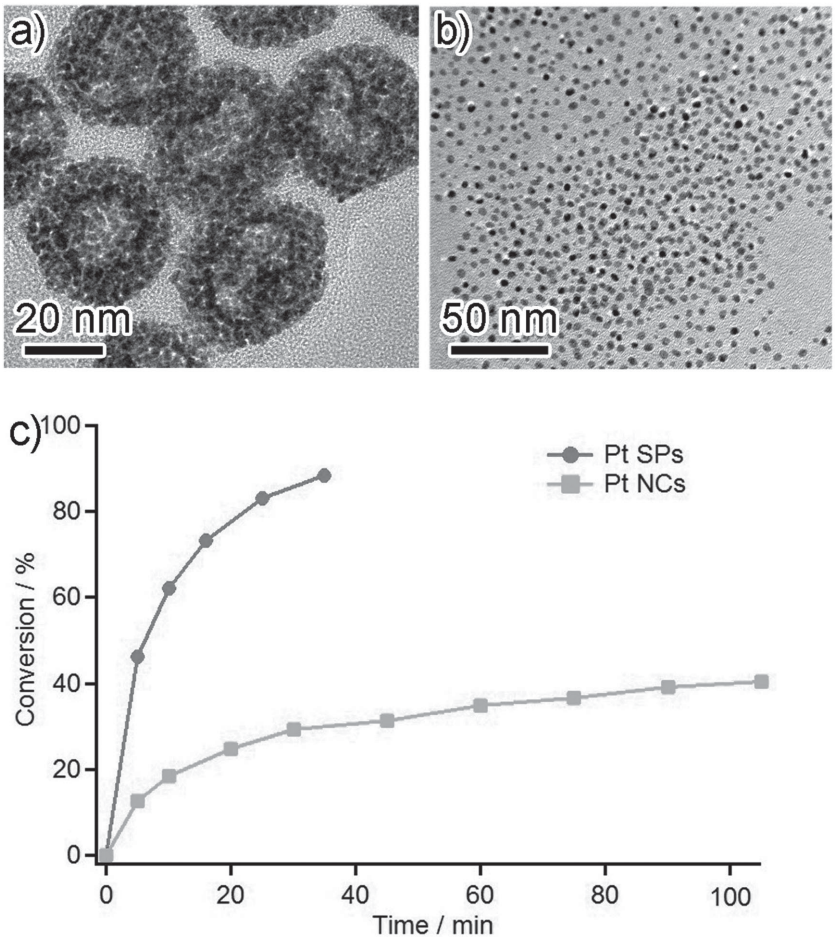

Figure 6. Performance evaluation of porous Pt CSPs in catalyzing electron transfer between $Fe(CN)_6^{3-}$ and $S_2O_3^{2-}$ in aqueous solutions. TEM images of a) porous Pt CSPs with averaged size of 34 nm and b) PAA-capped Pt nanocrystals with size of ≈4 nm. c) Conversion of hexacyanoferrate as a function of reaction time. The profiles labeled with circles and squares correspond to the reactions catalyzed with porous Pt CSPs and PAA-capped Pt nanocrystals, respectively. The progress of the reactions was monitored by the UV–vis–NIR spectrometer through analyzing the change of intensity at the peak position of 420 nm.

ligands, resulting clean surfaces with more accessible active sites for applications such as catalysis. The high-density negative charges due to the adsorption of halide ions enable excellent stability of the mesoporous CSPs in polar solvents (e.g., water and ethanol) that is beneficial for applications and post processing. Due to these advantages, the synthesized mesoporous Pt CSPs exhibit significantly improved catalytic activity and recyclability in catalyzing solution-phase electron-transfer reactions in comparison with the well-dispersed small Pt nanocrystals. As an emerging class of novel nanostructures, controlled synthesis of CSPs represents an important research area because of their unique properties originated from the coupling of individual nanocrystals in CSPs other than the intrinsic physical/chemical properties from the constituent nanocrystals. Assembly of the highly uniform CSPs into more complex and hierarchically ordered materials may enable the observation of new properties and the discovery of new applications.

4. Experimental Section

Chemicals: Ethanol (denatured), acetonitrile (HPLC grade), potassium iodide (KI, Granular), potassium ferricyanide (III) ($K_3Fe(CN)_6$), and ammonium hydroxide aqueous solution (28%) were purchased from Fisher Scientific. Sodium borohydride ($NaBH_4$, granules, 99.99% metals basis), sodium citrate tribasic dihydrate (99%), L-ascorbic acid (99+%, American Chemical Society (ACS) reagent), tetraethyl orthosilicate (98%), hydrogen tetrachloroaurate (III) trihydrate ($HAuCl_4{\cdot}3H_2O$, 99.9+%), sodium tetrachloroplatinate (II) hydrate ($Na_2PtCl_4{\cdot}xH_2O$), sodium tetrachloropalladate (II) (Na_2PdCl_4, 98%), sodium hexachlororhodate (III) (Na_3RhCl_6), sodium hexachloroiridate (III) hydrate ($Na_3IrCl_6{\cdot}xH_2O$), silver nitrate ($AgNO_3$, ≥ 99.0%), and PAA were purchased from Sigma-Aldrich. Silver powders (99.9%) were purchased from Strem Chemicals. Sodium thiosulfate ($Na_2S_2O_3$) was purchased from Alfa Aesar. All chemicals were used as received without further purification and treatment.

Synthesis of Ag Colloidal Nanoparticles: Ag colloidal particles with irregular shapes were prepared through the room-temperature reduction of $AgNO_3$ by ascorbic acid in deionized (DI) water containing acetonitrile. In a typical synthesis, DI water (20 mL) was first mixed with acetonitrile (5 mL). To this solution aqueous solutions of sodium citrate tribasic dihydrate (5 mL, 0.1 M) and ascorbic acid (2 mL, 0.1 M) were successively added. Injection of an aqueous solution of silver nitrate (5 mL, 0.01 M) to the solution initiated reduction reaction of Ag^+ ions. Lasting the reaction for 40 min resulted in the formation of irregularly shaped Ag colloidal nanoparticles with a broad size distribution ranging from 50 to 200 nm. Magnetic stirring was maintained throughout the entire synthesis. The Ag colloidal nanoparticles were then washed with water for two times and redispersed in water (36 mL) for future uses.

Synthesis of Pt–AgCl CSPs and Porous Pt CSPs: A 20-mL glass vial containing aqueous dispersion of the synthesized Ag colloidal nanoparticle (4 mL) and DI water (6 mL) was heated on a hot plate to boil the solution. To the boiling solution an aqueous solution of Na_2PtCl_4 (0.01 M) at a rate of 10 μL s^{-1} was added. After an appropriate amount of Na_2PtCl_4 solution was added, the reaction continued for additional 10 min. The reaction solution was kept boiling until the reaction stopped. The reaction solution was then cooled down in air and kept still for 0.5 h to precipitate large particle impurities. The light brown supernatant was finally collected, yielding a solution of Pt–AgCl composite CSPs. As for preparation of porous Pt CSPs, the collected solution of Pt–AgCl CSPs was centrifuged at 13 000 rpm for 10 min. The precipitate was redispersed in $NH_3{\cdot}H_2O$ (1.5 mL) and sonicated until a homogeneous dispersion was formed. The mixture was vortexed for 2 h to ensure the complete dissolution of AgCl. The resulting porous Pt CSPs were collected via centrifugation and water washing for three times. The Pt CSPs were finally dispersed in 2 mL DI water.

Synthesis of Composite RhI_3–AgI CSPs and IrI_3–AgI CSPs: A 20-mL glass vial containing aqueous dispersion of the synthesized Ag colloidal nanoparticle (4 mL), DI water (4 mL), and aqueous KI solution (0.1 M, 2 mL) was heated on a hot plate to boil the solution. To the boiling solution an aqueous solution of Na_3RhCl_6 (0.01 M) or Na_3IrCl_6 (0.01 M) at a rate of 10 μL s^{-1} was added. After an appropriate amount of Na_3RhCl_6 or Na_3IrCl_6 was added, the reaction continued for additional

10 min. The solution became dark brown for the reaction with Na_3RhCl_6 while the solution became deep orange for the reaction with Na_3IrCl_6. The reaction solution was then cooled down in air and kept still for 0.5 h to precipitate large particle impurities. The supernatant containing either RhI_3–AgI composite CSPs or IrI_3–AgI composite CSPs was collected.

Synthesis of Porous Rh and Ir CSPs: For the synthesis of porous Rh CSPs, the dispersion of RhI_3–AgI composite CSPs was centrifuged at 13 000 rpm for 10 min followed by washing with DI water for three times. The precipitated RhI_3–AgI CSPs were redispersed in 10 mL of DI water. To this CSP dispersion a freshly prepared aqueous solution of $NaBH_4$ (0.1 M, 300 µL) was added drop-by-drop. The color of the dispersion suddenly turned to light grey blue with a high grade of transparency. The resulting porous Rh CSPs were washed with DI water for three times and redispersed in ethanol (6 mL). To increase crystallinity of the porous Rh CSPs, the dispersion was thermally annealed at 150 °C and 41 psi for 20 min in a CEM Discover microwave reactor. The final product was centrifuged and redispersed in ethanol (3 mL) for further characterization. For the synthesis of porous Ir CSPs, the dispersion of IrI_3–AgI composite CSPs was centrifuged at 13 000 rpm for 10 min followed by washing with DI water for three times. The precipitated IrI_3–AgI CSPs were redispersed in 6 mL ethanol, which was thermally annealed at 150 °C and 40 psi for 20 min in a CEM Discover microwave reactor. The color changed from orange to light grey brown. The final product was centrifuged and redispersed in ethanol (3 mL) for further characterization.

Synthesis of Colloidal PAA-Capped Pt Nanocrystals: Pt nanocrystals were synthesized using a modified polyol process, in which Na_2PtCl_4 was reduced by ethylene glycol at elevated temperatures. In a typical synthesis, Na_2PtCl_4 (0.1 g) was dissolved in ethylene glycol (3 mL) at room temperature and this solution was then quickly injected to an ethylene glycol solution (15 mL) of PAA (0.030 M) that was preheated at 180 °C under a protective nitrogen atmosphere. The reaction lasted 20 min. Vigorous stirring was maintained throughout the entire reaction. The resulting nanoparticles were precipitated with acetone followed by centrifugation at 11 000 rpm. The nanoparticles were finally redispersed in DI water for characterization.

Reduction of $Fe(CN)_6^{3-}$ with $S_2O_3^{2-}$ Catalyzed by Porous Pt CSPs and Pt Nanocrystals: In a typical reaction, a dispersion (2.0 mL) of porous Pt CSPs and an aqueous dispersion of $K_3Fe(CN)_6$ (0.01 M, 0.1 mL) were added to a small glass vial. The catalytic reaction was initiated with the addition of an aqueous solution of $Na_2S_2O_3$ (0.1 M, 0.01 mL). A UV–vis spectrophotometer was used to monitor the reaction by recording the absorption at 420 nm, the absorption peak position of hexacyanoferrate(III) ions. When Pt nanocrystals were used as catalyst, the concentration of Pt nanocrystals was first adjusted to achieve same absorption spectrum as that of the porous Pt CSP dispersion. Similarly, a dispersion (2.0 mL) of Pt nanocrystals and an aqueous solution of $K_3Fe(CN)_6$ (0.01 M, 0.1 mL) were added to a small glass vial. The catalytic reaction was then initiated with the addition of an aqueous solution of $Na_2S_2O_3$ (0.1 M, 0.01 mL). The experiments were carried out at room temperature.

Characterization: TEM images were obtained on a JEOL 2010F transmission electron microscope operated at 200 kV. To prepare a TEM sample, a drop of particle dispersion was delivered to a carbon-coated copper grid with the use of pipette, followed by evaporation of solvent in air at room temperature. Energy dispersive X-ray spectra were collected with an INCA X-ray microanalysis system equipped on the JEOL 2010F(s) transmission electron microscope. A JSM JEOL 7500F field-emission scanning electron microscope operated at 10 kV under high-vacuum mode was used to record the SEM images. A VARIAN CARY-50 spectrophotometer was used to measure the UV–vis–NIR spectra of the particle dispersions. Bruker-VERTEX 7.0 FT-IR research spectrometer, which was equipped with Miracle-ATR single bounce, was used to record the IR absorption spectra. The Kratos AXIS-165 Surface Analysis System equipped for X-ray Photon Spectroscopy was used to analyze the chemical states and elemental compositions. The binding energy (BE) scale was calibrated relative to the BE of the C 1s peak (285.7 eV). Curve fitting analysis of the core level spectra was based on the summed Gaussian/Lorentzian GL functions, with a Shirley-type background subtraction. XRD patterns were acquired using a Bruker D2 Phaser X-ray diffractometer operating at 30 kV with a current of 10 mA. The X-ray source was Cu $K_{\alpha 1}$ radiation with a wavelength of 1.5406 Å.

Supporting Information

Supporting Information is available from the Wiley Online Library or from the author.

Acknowledgements

This work was performed at the Center for Nanoscale Materials, a U.S. Department of Energy, Office of Science, Office of Basic Energy Sciences User Facility under Contract No. DE-AC02-06CH11357. The authors thank Dr. Zheng Li for help.

Received: October 20, 2014
Revised: December 22, 2014
Published online: January 23, 2015

[1] X. Hu, J. Gong, L. Zhang, J. C. Yu, *Adv. Mater.* **2008**, *20*, 4845.
[2] H. Kim, J. Ge, J. Kim, S.-E. Choi, H. Lee, H. Lee, W. Park, Y. Yin, S. Kwon, *Nat. Photonics* **2009**, *3*, 534.
[3] B. Abécassis, M. D. Tessier, P. David, B. Dubertret, *Nano Lett.* **2014**, *14*, 710.
[4] J. Zhuang, A. D. Shaller, J. Lynch, H. Wu, O. Chen, A. D. Q. Li, Y. C. Cao, *J. Am. Chem. Soc.* **2009**, *131*, 6084.
[5] Q. Lu, Z. Lu, Y. Lu, L. Lv, Y. Ning, H. Yu, Y. Hou, Y. Yin, *Nano Lett.* **2013**, *13*, 5698.
[6] Z. Lu, M. Ye, N. Li, W. Zhong, Y. Yin, *Angew. Chem. Int. Ed.* **2010**, *49*, 1862.
[7] Z. Lu, Y. Yin, *Chem. Soc. Rev.* **2012**, *41*, 6874.
[8] D. J. Milliron, R. Buonsanti, A. Llordes, B. A. Helms, *Acc. Chem. Res.* **2014**, *47*, 236.
[9] T. Wang, D. LaMontagne, J. Lynch, J. Zhuang, Y. C. Cao, *Chem. Soc. Rev.* **2013**, *42*, 2804.
[10] T. Wang, X. Wang, D. LaMontagne, Z. Wang, Z. Wang, Y. C. Cao, *J. Am. Chem. Soc.* **2012**, *134*, 18225.
[11] Y. Xia, N. Trung Dac, M. Yang, B. Lee, A. Santos, P. Podsiadlo, Z. Tang, S. C. Glotzer, N. A. Kotov, *Nat. Nanotechnol.* **2011**, *6*, 580.
[12] S. A. Jenekhe, X. L. Chen, *Science* **1998**, *279*, 1903.
[13] Z. Nie, D. Fava, E. Kumacheva, S. Zou, G. C. Walker, M. Rubinstein, *Nat. Mater.* **2007**, *6*, 609.
[14] A. K. Boal, F. Ilhan, J. E. DeRouchey, T. Thurn-Albrecht, T. P. Russell, V. M. Rotello, *Nature* **2000**, *404*, 746.
[15] R. Klajn, K. J. M. Bishop, M. F. Maciej Paszewski, C. J. Campbell, T. P. Gray, B. A. Grzybowski, *Science* **2007**, *316*, 261.
[16] F. Bai, D. Wang, Z. Huo, W. Chen, L. Liu, X. Liang, C. Chen, X. Wang, Q. Peng, Y. Li, *Angew. Chem. Int. Ed.* **2007**, *46*, 6650.
[17] Y. Liu, D. Wang, Q. Peng, D. Chu, X. Liu, Y. Li, *Inorg. Chem.* **2011**, *50*, 5841.
[18] J. Zhuang, H. Wu, Y. Yang, Y. C. Cao, *J. Am. Chem. Soc.* **2007**, *129*, 14166.
[19] J. Zhuang, H. Wu, Y. Yang, Y. C. Cao, *Angew. Chem. Int. Ed.* **2008**, *47*, 2208.
[20] T. Wang, J. Zhuang, J. Lynch, O. Chen, Z. Wang, X. Wang, D. LaMontagne, H. Wu, Z. Wang, Y. C. Cao, *Science* **2012**, *338*, 358.
[21] T. Wang, X. Wang, D. LaMontagne, Z. Wang, Y. C. Cao, *J. Am. Chem. Soc.* **2013**, *135*, 6022.
[22] D. Wang, T. Xie, Q. Peng, Y. Li, *J. Am. Chem. Soc.* **2008**, *130*, 4016.

[23] J. Lacava, P. Born, T. Kraus, *Nano Lett.* **2012**, *12*, 3279.
[24] J. Han, X. Zhang, Y. Zhou, Y. Ning, J. Wu, S. Liang, H. Sun, H. Zhang, B. Yang, *J. Mater. Chem.* **2012**, *22*, 2679.
[25] M. M. Maye, I.-I. S. Lim, J. Luo, Z. Rab, D. Rabinovich, T. Liu, C.-J. Zhong, *J. Am. Chem. Soc.* **2005**, *127*, 1519.
[26] J. Ge, Y. Hu, M. Biasini, P. W. Beyermann, Y. Yin, *Angew. Chem. Int. Ed.* **2007**, *46*, 4342.
[27] Y. Sun, Y. Xia, *Adv. Mater.* **2004**, *16*, 264.
[28] Y. Sun, Y. Xia, *Adv. Mater.* **2003**, *15*, 695.
[29] T. K. Sau, C. J. Murphy, *J. Am. Chem. Soc.* **2004**, *126*, 8648.
[30] B. T. Sneed, C.-H. Kuo, C. N. Brodsky, C.-K. Tsung, *J. Am. Chem. Soc.* **2012**, *134*, 18417.
[31] R. B. Bedford, S. L. Hazelwood, *Organometallics* **2002**, *21*, 2599.
[32] S. Boverie, F. Simal, A. Demonceau, A. F. Noels, I. L. Eremenko, A. A. Sidorov, S. E. Nefedov, *Tetrahedron Lett.* **1997**, *38*, 7543.
[33] Y. Li, J. Petroski, M. A. El-Sayed, *J. Phys. Chem. B* **2000**, *104*, 10956.
[34] A. Dandapat, D. Jana, G. De, *ACS Appl. Mater. Interfaces* **2009**, *1*, 833.
[35] M. A. Mahmoud, B. Snyder, M. A. El-Sayed, *J. Phys. Chem. Lett.* **2010**, *1*, 28.
[36] H. Li, M. Cao, T. Liu, R. Cao, *J. Colloid Interface Sci.* **2012**, *369*, 352.
[37] G. W. Qin, W. Pei, X. Ma, X. Xu, Y. Ren, W. Sun, L. Zuo, *J. Phys. Chem. C* **2010**, *114*, 6909.
[38] A. M. Kalekar, K. K. Sharma, A. Lehoux, F. Audonnet, H. Remita, A. Saha, G. K. Sharma, *Langmuir* **2013**, *29*, 11431.